Theoretical Chemistry Accounts (2026) 145:43
https://doi.org/10.1007/s00214-026-03288-8

RESEARCH

The relativistic hydrogen-like atom in a finite magnetic field

Benedikt Menges[1] · Bang C. Huynh[2] · Lucas Visscher[1] · Ansgar Pausch[1]

Received: 26 January 2026 / Accepted: 3 March 2026

Abstract
This work focuses on developing an efficient numerical method to solve the relativistic hydrogen-like atom in a finite magnetic field. To this end, we derive and implement an algorithm based on Gaussian-type orbitals that exploits fermionic symmetry to accelerate the calculations and to distinguish states of different character. This is then used to investigate a novel type of mixing regime between internal and external magnetic interactions. Finally, we assess the implications for the core region of heavy elements, where spin-orbit coupling is much stronger than the effects of external magnetic fields, and the consequences for quantum chemical calculations on heavy atoms in the vicinity of white dwarfs.

Keywords Magnetic fields · Relativistic effects · Heavy elements · Symmetry

1 Introduction

The effects of external magnetic fields on atoms have been studied extensively for well over a century, both experimentally and with the use of computational methods [1, 2]. From a chemical perspective, the interaction between electrons in an atom and external magnetic fields is of considerable interest. Many important phenomena are related to this interaction and are widely studied in fields ranging from experimental physics [3–6] to biochemistry [7–10]. In non-relativistic quantum chemistry, these effects can be modeled by augmenting the Hamiltonian $\hat{H}$ to include an interaction term with the external magnetic field,

$$\hat{H} = \hat{H}^0 + \hat{H}^{\text{int}}(\mathbf{B}) \,, \tag{1}$$

and solving the corresponding Schrödinger equation [11]. Conventionally, this is done by first solving the stationary Schrödinger equation for the unperturbed Hamiltonian $\hat{H}^0$ and subsequently applying (linear) perturbation theory to model the effects of the external magnetic field $\mathbf{B}$ in the interaction Hamiltonian $\hat{H}^{\text{int}}$ [12]. This has been an incredibly successful approach for many decades and is widely used to facilitate the ab initio calculation of magnetic properties and spectroscopic data [13–17].

The reason for this success is quite simple: the Coulomb forces which govern the electronic structure of atoms and molecules are orders of magnitude larger than the effects of any magnetic field we can currently create on Earth [18]. Only in very exotic environments such as the vicinity of magnetic white dwarfs can magnetic fields become strong enough to compete with intra-atomic Coulomb forces [19–23]. In such cases, the magnetic field strength is treated as a parameter and the Schrödinger equation for the total Hamiltonian in Eq. (1) is solved for a finite field [24, 25]. Since atomic spectra obtained from magnetic white dwarfs can only be interpreted if reference data from quantum chemical calculations is available, the finite magnetic field approach has become increasingly popular in recent years [26–28]. However, recent work within this field has noted that in order to describe some heavier elements such as calcium in the presence of external magnetic fields accurately enough, the interplay between relativistic effects and magnetic fields will have to be accounted for [29].

In relativistic theory, the picture becomes more complicated. Here, the electronic structure of atoms is governed by the full electromagnetic interaction, which is typically divided into an electric part (scalar-relativistic) and a magnetic part (spin-orbit coupling, Breit interaction). As such, an external magnetic field competes not only with Coulomb forces but also with the internal magnetic field of an atom.

✉ Ansgar Pausch
a.i.pausch@vu.nl

[1] Department of Chemistry and Pharmaceutical Sciences, Vrije Universiteit Amsterdam, De Boelelaan 1108, 1081 HZ Amsterdam, The Netherlands

[2] Physical and Theoretical Chemistry Laboratory, Department of Chemistry, University of Oxford, Oxford OX1 3QZ, UK

Published online: 20 April 2026

The Dirac Hamiltonian $\hat{H}^{\mathrm{D}}$ may accordingly be divided into three parts:

$$\hat{H}^{\mathrm{D}} = \hat{H}^{0,\mathrm{el}} + \hat{H}^{0,\mathrm{mag}} + \hat{H}^{\mathrm{int}}(\mathbf{B})\,. \tag{2}$$

Compared to the unperturbed non-relativistic Hamiltonian $\hat{H}^0$ in Eq. (1), the unperturbed Dirac Hamiltonian in Eq. (2) contains an electric $\hat{H}^{0,\mathrm{el}}$ and a magnetic $\hat{H}^{0,\mathrm{mag}}$ contribution. Crucially, non-linear interactions need not arise solely when the effects of the magnetic field compete with the electronic part of the Dirac Hamiltonian, which is mostly relevant to the aforementioned exotic environments. Instead, the competition between internal and external magnetic interactions can also give rise to a variety of interesting phenomena. Depending on the strength of magnetic contributions such as spin-orbit coupling (SOC), such non-linear interactions can, in principle, occur at any magnetic field strength.

The important limits of this interaction are well-documented from experimental data. The *anomalous Zeeman effect* is used to describe systems in which the SOC is much stronger than the external field, while the *Paschen–Back limit* is relevant for systems in which the external magnetic field is much stronger than the SOC. On the other hand, if both internal and external magnetic effects are of similar magnitude, a new type of mixing regime emerges that has not been thoroughly explored by computational methods. Even for the simplest system—the relativistic hydrogen-like atom in a uniform, static magnetic field—analytical solutions are available only for states of certain symmetry (Breit–Rabi formula) [30]. Furthermore, as far as we are aware, there exist very few numerical implementations for relativistic quantum chemistry in finite magnetic fields [31–33]. To the best of our knowledge, these implementations are not capable of exploiting fermionic symmetry and they are directly embedded into a many-electron framework. Therefore, they cannot be used for precise calculations on one-electron systems that require very large basis sets.

In this work, we explore the non-linear interaction between various relativistic hydrogen-like atoms and external magnetic fields. To this end, we employ a numerical implementation capable of solving the Dirac equation with large, even-tempered basis sets consisting of angular momentum quantum numbers up to $l_{\mathrm{max}} = 18$ to account for the increasingly cylindrical shapes of the spinors [34, 35]. Existing symmetries, namely inversion parity and total angular momentum projection along the magnetic field axis, are exploited to accelerate the calculations and to classify the solutions properly. Of particular interest for this investigation are regions in which the effects of the external magnetic field are comparable in magnitude to those of SOC. For atoms with an increasing nuclear charge, this is expected to be the case in stronger magnetic fields. As such, we investigate these effects for H, Li^{2+}, Na^{10+}, K^{18+}, Cu^{28+}, Ag^{46+}, Au^{78+}, and Rn^{85+}.

2 Theory

2.1 Preface and notations

We begin by introducing our formalism and notations. Throughout this article, we work in the adiabatic limit of the Born–Oppenheimer (BO) approximation. We use Hartree atomic units throughout unless stated otherwise: $\hbar = m_{\mathrm{e}} = e = 4\pi\varepsilon_0 = 1$. The speed of light in vacuum is denoted as c. We use bold-face letters such as $\mathbf{S}$ for two-component (2C) matrices and italic letters such as S for one-component (1C) matrices. The traceless Pauli matrices compose a vector $\boldsymbol{\sigma} = (\sigma_x, \sigma_y, \sigma_z)^\top$, and σ_0 is the 2C identity matrix. We write δ_{ij} for the Kronecker delta and ε_{ijk} for the Levi–Civita symbol.

2.2 Modified Dirac equation with the restricted magnetic balance condition

The energy levels of the relativistic hydrogen-like atom can be obtained from the solutions to the Dirac equation:

$$\hat{H}^{\mathrm{D}}|\Psi_p\rangle = E_p|\Psi_p\rangle\,, \tag{3}$$

which is conventionally shifted in its potential energy to align with the non-relativistic solutions. The Dirac Hamiltonian $\hat{H}^{\mathrm{D}}$ is a four-component (4C) operator and the corresponding wave functions Ψ can describe both electronic and positronic motion. In this work, we focus on the positive (p) energy solutions (corresponding to electrons) and neglect all solutions lower than $-2c^2$. Thus, the subscript p in the wave function and the energy E_p refers exclusively to an electronic state here. The wave function is commonly separated into so-called large (L) and small (S) components, and the Dirac equation is then expressed as

$$\begin{pmatrix} \hat{V} & c\,\boldsymbol{\sigma}\cdot\hat{\boldsymbol{\pi}} \\ c\,\boldsymbol{\sigma}\cdot\hat{\boldsymbol{\pi}} & -2c^2 + \hat{V} \end{pmatrix} \begin{pmatrix} \Psi_p^{\mathrm{L}} \\ \Psi_p^{\mathrm{S}} \end{pmatrix} = E_p \begin{pmatrix} \Psi_p^{\mathrm{L}} \\ \Psi_p^{\mathrm{S}} \end{pmatrix}. \tag{4}$$

For a hydrogen-like atom in the adiabatic BO approximation, the potential energy operator $\hat{V}$ corresponds to the nuclear attraction and $\hat{\boldsymbol{\pi}}$ is the kinetic momentum operator. In the presence of an external magnetic field, the kinetic momentum operator is constructed via minimal coupling,

$$\hat{\boldsymbol{\pi}} = \hat{\mathbf{p}} + \mathbf{A}_{\mathbf{O}}(\mathbf{r})\,, \tag{5}$$

from the canonical momentum operator $\hat{\mathbf{p}} = -\mathrm{i}\nabla$ and a vector potential $\mathbf{A}_{\mathbf{O}}(\mathbf{r})$. In a uniform static magnetic field,

the latter can be written as:

$$\mathbf{A_O}(\mathbf{r}) = \frac{1}{2}\mathbf{B} \times (\mathbf{r} - \mathbf{O}) , \tag{6}$$

where $\mathbf{r}$ corresponds to the electronic coordinate and $\mathbf{O}$ is an arbitrarily chosen gauge origin. For atomic systems within the BO approximation, the nucleus is commonly placed at the gauge origin, a choice referred to as the natural gauge. In this work, we expand the wave function in a finite basis set and adopt the restricted magnetic balance (RMB) condition to avoid variational collapse: [36–38]

$$|\Psi_p^{\mathrm{L}}\rangle = \sum_\mu C_{p\mu}^{\mathrm{L}} |\mu\rangle , \tag{7}$$

$$|\Psi_p^{\mathrm{S}}\rangle = \sum_\mu C_{p\mu}^{\mathrm{S}} \frac{\boldsymbol{\sigma}\cdot\hat{\boldsymbol{\pi}}}{2c} |\mu\rangle . \tag{8}$$

The basis functions $|\mu\rangle$ are London atomic orbitals (LAOs) [2, 39], which are constructed from Gaussian-type orbitals (GTOs). We will further discuss these basis functions in Sect. 2.3. Spinor coefficients for the large and small components $\mathbf{C}^{\mathrm{L/S}}$ are two-component quantities. The modified Dirac equation expressed in a finite basis constrained by the RMB condition can be written as [32]

$$\begin{pmatrix} \mathbf{V} & \mathbf{\Pi} \\ \mathbf{\Pi} & \frac{1}{4c^2}\mathbf{W} - \mathbf{\Pi} \end{pmatrix} \begin{pmatrix} \mathbf{C}_p^{\mathrm{L}} \\ \mathbf{C}_p^{\mathrm{S}} \end{pmatrix} = E_p \begin{pmatrix} \mathbf{S} & \mathbf{0} \\ \mathbf{0} & \frac{1}{2c^2}\mathbf{\Pi} \end{pmatrix} \begin{pmatrix} \mathbf{C}_p^{\mathrm{L}} \\ \mathbf{C}_p^{\mathrm{S}} \end{pmatrix} . \tag{9}$$

The overlap $\mathbf{S}$ and potential energy $\mathbf{V}$ matrices are constructed from their 1C non-relativistic counterparts:

$$\mathbf{S}_{\mu\nu} = \sigma_0 \langle\mu|\nu\rangle = \sigma_0 S_{\mu\nu} , \tag{10}$$

$$\mathbf{V}_{\mu\nu} = \sigma_0 \langle\mu|\hat{V}|\nu\rangle = \sigma_0 V_{\mu\nu} . \tag{11}$$

Both the kinetic energy $\mathbf{\Pi}$ and the relativistically modified potential $\mathbf{W}$ are expressed in the 2C basis:

$$\mathbf{\Pi}_{\mu\nu} = \frac{1}{2}\langle\mu|(\boldsymbol{\sigma}\cdot\hat{\boldsymbol{\pi}})(\boldsymbol{\sigma}\cdot\hat{\boldsymbol{\pi}})|\nu\rangle , \tag{12}$$

$$\mathbf{W}_{\mu\nu} = \langle\mu|(\boldsymbol{\sigma}\cdot\hat{\boldsymbol{\pi}})\hat{V}(\boldsymbol{\sigma}\cdot\hat{\boldsymbol{\pi}})|\nu\rangle . \tag{13}$$

However, it is possible to deconstruct both of them into 1C contributions using the Dirac identity

$$(\boldsymbol{\sigma}\cdot\hat{\mathbf{a}})(\boldsymbol{\sigma}\cdot\hat{\mathbf{b}}) = (\hat{\mathbf{a}}\cdot\hat{\mathbf{b}})\sigma_0 + \mathrm{i}\,(\hat{\mathbf{a}}\times\hat{\mathbf{b}})\cdot\boldsymbol{\sigma} , \tag{14}$$

which leads to the following form for the kinetic energy matrix:

$$\mathbf{\Pi} = \begin{pmatrix} \Pi_0 + \mathrm{i}\Pi_z & \Pi_y + \mathrm{i}\Pi_x \\ -\Pi_y + \mathrm{i}\Pi_x & \Pi_0 - \mathrm{i}\Pi_z \end{pmatrix} . \tag{15}$$

The 1C matrices can then be constructed from

$$\begin{aligned} \Pi_{0,\mu\nu} &= \frac{1}{2}\langle\mu|\hat{\pi}_x^2 + \hat{\pi}_y^2 + \hat{\pi}_z^2|\nu\rangle := T_{\mu\nu} , \\ \Pi_{x,\mu\nu} &= \frac{1}{2}\langle\mu|\hat{\pi}_y\hat{\pi}_z - \hat{\pi}_z\hat{\pi}_y|\nu\rangle = -\frac{\mathrm{i}B_x}{2} S_{\mu\nu} , \\ \Pi_{y,\mu\nu} &= \frac{1}{2}\langle\mu|\hat{\pi}_z\hat{\pi}_x - \hat{\pi}_x\hat{\pi}_z|\nu\rangle = -\frac{\mathrm{i}B_y}{2} S_{\mu\nu} , \\ \Pi_{z,\mu\nu} &= \frac{1}{2}\langle\mu|\hat{\pi}_x\hat{\pi}_y - \hat{\pi}_y\hat{\pi}_x|\nu\rangle = -\frac{\mathrm{i}B_z}{2} S_{\mu\nu} . \end{aligned} \tag{16}$$

Therein, we have defined a scalar kinetic energy contribution T, which also contains the well-known orbital Zeeman and diamagnetic terms. The other three contributions Π_x, Π_y, and Π_z can be identified as the spin Zeeman terms. Using the definitions in Eq. (16), we may write the 2C kinetic energy contribution as

$$\mathbf{\Pi} = \begin{pmatrix} T + \frac{1}{2}B_z\, S & \frac{1}{2}[B_x - \mathrm{i}B_y]S \\ \frac{1}{2}[B_x + \mathrm{i}B_y]S & T - \frac{1}{2}B_z\, S \end{pmatrix} . \tag{17}$$

The 2C relativistically modified potential can be decomposed in a similar manner:

$$\mathbf{W} = \begin{pmatrix} W_0 + \mathrm{i}W_z & W_y + \mathrm{i}W_x \\ -W_y + \mathrm{i}W_x & W_0 - \mathrm{i}W_z \end{pmatrix} . \tag{18}$$

Its individual 1C contributions are computed as

$$\begin{aligned} W_{0,\mu\nu} &= \langle\mu|\hat{\pi}_x\hat{V}\hat{\pi}_x + \hat{\pi}_y\hat{V}\hat{\pi}_y + \hat{\pi}_z\hat{V}\hat{\pi}_z|\nu\rangle , \\ W_{x,\mu\nu} &= \langle\mu|\hat{\pi}_y\hat{V}\hat{\pi}_z - \hat{\pi}_z\hat{V}\hat{\pi}_y|\nu\rangle , \\ W_{y,\mu\nu} &= \langle\mu|\hat{\pi}_z\hat{V}\hat{\pi}_x - \hat{\pi}_x\hat{V}\hat{\pi}_z|\nu\rangle , \\ W_{z,\mu\nu} &= \langle\mu|\hat{\pi}_x\hat{V}\hat{\pi}_y - \hat{\pi}_y\hat{V}\hat{\pi}_x|\nu\rangle , \end{aligned} \tag{19}$$

which are conveniently expressed as linear combinations of potential energy integrals. To summarize, the modified Dirac equation can be expressed in a finite basis using the RMB condition [36–38]. Only 1C matrices containing integrals over GTOs have to be evaluated. From these, all 2C and 4C matrices can be constructed.

2.3 Basis set requirements and gauge transformation

We use LAOs as basis functions to ensure gauge invariance. They are defined as [2, 12]

$$|\mu\rangle := e^{-\frac{\mathrm{i}}{2}\mathbf{B}\times(\mathbf{R}^\mu - \mathbf{O})\cdot\mathbf{r}} \chi_\mu(\mathbf{r}) , \tag{20}$$

where $\mathbf{R}^\mu$ is the position of the nucleus and χ_μ is a GTO. In the context of this work, we work in the natural gauge ($\mathbf{R}^\mu = \mathbf{O}$) [40], which is also chosen to coincide with the origin of the coordinate system. In the natural gauge, LAOs

are then equivalent to GTOs, which can be expressed in the Cartesian form as

$$\chi_\mu(\mathbf{r}) = N_\mu x^{a_x^\mu} y^{a_y^\mu} z^{a_z^\mu} e^{-\zeta_\mu r^2} . \tag{21}$$

Please note that our implementation is in principle not limited to the natural gauge, as we use a LAO integral code basis [41]. The type of function is defined by the angular momentum vector $\mathbf{l}_\mu = (a_x^\mu, a_y^\mu, a_z^\mu)^\top$, with $l_\mu \equiv a_x^\mu + a_y^\mu + a_z^\mu = 0, 1, 2, \ldots$ corresponding to Cartesian $s, p, d, \ldots$ functions, respectively. The normalization constant is denoted as N_μ and the exponents ζ_μ are held constant during the calculation. Large even-tempered basis sets are used throughout this work for which the exponents are chosen as

$$\zeta_i = \zeta_{\min} \cdot \Delta^i , \tag{22}$$

with $i \in \mathbb{N}_0$ and $\Delta \in \mathbb{R}^+$ such that all $\zeta_i \leq \zeta_{\max}$. Please note that the choice of $\zeta_{\min}$, $\zeta_{\max}$, and Δ uniquely defines the basis set. Integrals are calculated in the Cartesian GTO basis. Compared to the non-relativistic case, only integrals for the relativistically modified potential are additionally required. As shown above, these can be decomposed into integrals of the type $\langle\mu|\hat{\pi}_\alpha \hat{V} \hat{\pi}_\beta|\nu\rangle$ and require us to evaluate

$$\begin{aligned}\hat{\pi}_\alpha|\mu\rangle = &-\mathrm{i}\, a_\alpha^\mu|\mu - 1_\alpha\rangle + 2\mathrm{i}\,\zeta_\mu|\mu + 1_\alpha\rangle \\ &+ \frac{1}{2}\sum_{\beta\gamma} \varepsilon_{\alpha\beta\gamma} B_\beta |\mu + 1_\gamma\rangle ,\end{aligned} \tag{23}$$

with $\alpha, \beta, \gamma \in \{x, y, z\}$. Finally, all relevant integrals have to be transformed into the basis of Laplace's spherical harmonics [42]:

$$\tilde{\chi}_\mu(\mathbf{r}) = \tilde{N}_\mu Y_l^{m_l} r^n e^{-\zeta_\mu r^2} . \tag{24}$$

Therein, n is the principal quantum number, l the angular momentum quantum number, and m_l the angular momentum projection along the z-axis (which is the eigenvalue of the $\hat{l}_z$ operator). For each $l = l_\mu$, the spherical harmonics $\tilde{\chi}_\mu$ in Eq. (24) span a subspace of the Cartesian functions χ_μ in Eq. (21) and also form an orthonormal basis with respect to both l and m_l due to

$$\langle Y_l^{m_l} | Y_{l'}^{m_l'} \rangle = \delta_{ll'}\delta_{m_l m_l'} . \tag{25}$$

2.4 Symmetry classification of one-electron relativistic states in a hydrogen-like system

The unitary symmetry point group of an atom or ion in a uniform external magnetic field is $\mathcal{C}_{\infty h}$ [43–46]. Wave functions describing a single electron in such an atom or ion must transform as one of the projective [44, 47] (or fermionic, or double-valued) irreducible representations of $\mathcal{C}_{\infty h}$ which must all be one-dimensional since $\mathcal{C}_{\infty h}$ (and its double-group equivalent) is Abelian [45]. Each eigenfunction $|\Psi_p\rangle$ in Eq. (3) is therefore non-degenerate for $|\mathbf{B}| > 0$, and we seek to determine the projective irreducible representation of $\mathcal{C}_{\infty h}$ as which $|\Psi_p\rangle$ transforms.

It is well-known that each relativistic state of the electron in a hydrogen-like atom in the absence of an external magnetic field is characterized by three quantum numbers: l, j, and m_j (which is the eigenvalue of the $\hat{j}_z$ operator) [48]. For convenience, we shall define another quantum number $a = 2(l - j)$ which has only two possible values, ± 1. Please note the similarities to the quantum number $\kappa = 2(l - j)(j + 1/2)$ used elsewhere in the literature [49], which implies $a = \mathrm{sgn}(\kappa)$ [48]. This allows us to write each relativistic state of the electron in a hydrogen-like atom compactly as

$$|j, m_j\rangle^a = \begin{cases} |j, m_j\rangle^+ \equiv |l = j + 1/2, j, m_j\rangle , \\ |j, m_j\rangle^- \equiv |l = j - 1/2, j, m_j\rangle . \end{cases} \tag{26}$$

When a uniform magnetic field is introduced, all degeneracy exhibited by $|j, m_j\rangle^a$ is lifted. Consequently, l and j are no longer good quantum numbers in the sense that they do not uniquely identify the projective irreducible representations of $\mathcal{C}_{\infty h}$ spanned by $|j, m_j\rangle^a$. On the other hand, as shall be further explained in Sect. 2.5, m_j is still a good quantum number, as is the inversion parity $\mathcal{P} = (-1)^l$, and we thus expect that they together characterize the symmetry of $|j, m_j\rangle^a$ in $\mathcal{C}_{\infty h}$. In fact, to quantify this, we show in the last two rows of Table 1 the characters of $|j, m_j\rangle^a$ in $\mathcal{C}_{\infty h}$, the derivation of which is presented in the Supporting Information. A careful consideration of these characters shows that each of the following series

$$|j, m_j\rangle^+, |j + 1, m_j\rangle^-, |j + 2, m_j\rangle^+, |j + 3, m_j\rangle^-, \ldots$$

and

$$|j, m_j\rangle^-, |j + 1, m_j\rangle^+, |j + 2, m_j\rangle^-, |j + 3, m_j\rangle^+, \ldots$$

contains states that transform according to the same projective irreducible representation of $\mathcal{C}_{\infty h}$ and can thus mix with each other via $\hat{H}^{\mathrm{D}}$ to yield $|\Psi_p\rangle$ as described in Sect. 2.6. Each series is uniquely specified by the value of m_j and the parity of $l = j \pm 1/2$ and assignable to one of the projective irreducible representations of $\mathcal{C}_{\infty h}$ whose characters are also shown in Table 1 [45]. These shall be used to label the computed $|\Psi_p\rangle$ states that we present in Sect. 4.

Table 1 Characters of projective irreducible representations and of $|j, m_j\rangle^a$ in $\mathcal{C}_{\infty h}$. The projective irreducible representations are enumerated by $|m_j|$ which is a positive half-integer

$\mathcal{C}_{\infty h}$	E	$C_z(\phi)$	i	σ_h	$S_z(\phi)$
$E^+_{\lvert m_j\rvert,g}$	$+1$	$e^{+\mathrm{i}\phi\lvert m_j\rvert}$	$+1$	$+\mathrm{i}$	$-\mathrm{i}e^{+\mathrm{i}\phi\lvert m_j\rvert}$
$E^-_{\lvert m_j\rvert,g}$	$+1$	$e^{-\mathrm{i}\phi\lvert m_j\rvert}$	$+1$	$-\mathrm{i}$	$+\mathrm{i}e^{-\mathrm{i}\phi\lvert m_j\rvert}$
$E^+_{\lvert m_j\rvert,u}$	$+1$	$e^{+\mathrm{i}\phi\lvert m_j\rvert}$	-1	$-\mathrm{i}$	$+\mathrm{i}e^{+\mathrm{i}\phi\lvert m_j\rvert}$
$E^-_{\lvert m_j\rvert,u}$	$+1$	$e^{-\mathrm{i}\phi\lvert m_j\rvert}$	-1	$+\mathrm{i}$	$-\mathrm{i}e^{-\mathrm{i}\phi\lvert m_j\rvert}$
$\lvert j, m_j\rangle^+$	$+1$	$e^{-\mathrm{i}\phi m_j}$	$(-1)^{j+1/2}$	$(-1)^{j+1/2-m_j}$	$-(-1)^{j+1/2-m_j}e^{-\mathrm{i}\phi m_j}$
$\lvert j, m_j\rangle^-$	$+1$	$e^{-\mathrm{i}\phi m_j}$	$(-1)^{j-1/2}$	$(-1)^{j-1/2-m_j}$	$-(-1)^{j-1/2-m_j}e^{-\mathrm{i}\phi m_j}$

2.5 Symmetry transformation of the Dirac Hamiltonian

In order to accelerate the calculations and retain information about the symmetry of the solutions, we use a symmetry-transformed Dirac Hamiltonian. Due to the presence of the external magnetic field, time-reversal symmetry is not preserved and the Dirac Hamiltonian $\hat{H}^{\mathrm{D}}$ can only be decomposed using complex-quaternionic algebra according to Ref. [50]. Instead of such an approach, we exploit the individual symmetries that remain preserved in the presence of a magnetic field via the unitary point group $\mathcal{C}_{\infty h}$. This includes the spatial inversion i:

$$\left[\hat{H}^{\mathrm{D}}, \hat{i}\right] = 0. \tag{28}$$

For the states $|j, m_j\rangle^{\pm} \equiv |l = j \pm 1/2, j, m_j\rangle$ which are indeed eigenfunctions of $\hat{i}$, the associated eigenvalues $\mathcal{P} = (-1)^l$ are referred to as their *inversion parities*. These can be either $+1$ for *gerade* states or -1 for *ungerade* states. Since we use a basis of spherical harmonics, the respective symmetry transformation of the Dirac Hamiltonian in this basis is rather straightforward: the Dirac Hamiltonian can be decomposed into two blocks corresponding to *gerade* ($s, d, \ldots$) and *ungerade* ($p, f, \ldots$) basis functions. This parity partitioning is depicted in Fig. 1.

Furthermore, as the magnetic field is applied in the Cartesian z-direction, there are infinitely many $C_z(\phi)$ rotations for $\phi \in (-\pi, \pi]$ that commute with $\hat{H}^{\mathrm{D}}$. Since these rotations can all be generated by $\hat{j}_z$, the total angular momentum projection along the z-axis, we can write

$$\left[\hat{H}^{\mathrm{D}}, \hat{j}_z\right] = 0 \tag{29}$$

and hence recognize that m_j is a good quantum number. The 4C $\hat{j}_z$ operator can be written as

$$\hat{j}_z = \begin{pmatrix} \hat{l}_z + \frac{1}{2}\sigma_z & 0 \\ 0 & \hat{l}_z + \frac{1}{2}\sigma_z \end{pmatrix} \tag{30}$$

and its eigenvectors in a basis consisting of spherical harmonics up to some maximum degree $l_{\max}$ can be precomputed once and used for all subsequent calculations. Following the block-diagonal structure of $\hat{j}_z$, this may be done by constructing a basis consisting of a single set of $s, p, d, \ldots$ functions and solving the following generalized eigenvalue equation:

$$\mathbf{J}_z \mathbf{C}_{j_z} = \mathbf{m}_j \mathbf{S} \mathbf{C}_{j_z}\,. \tag{31}$$

The diagonal matrix $\mathbf{m}_j$ contains the eigenvalues of the 2C matrix $\mathbf{J}_z$, which are often denoted as m_j. It can be conveniently decomposed into an orbital and a spin contribution according to:

$$\mathbf{J}_z = \sigma_0 L_z + \frac{1}{2}\sigma_z S\,, \tag{32}$$

with individual elements of matrix L_z being constructed from

$$L_{z,\mu\nu} = \left\langle \mu \middle| -\mathrm{i}\left(x\frac{\partial}{\partial y} - y\frac{\partial}{\partial x}\right) \middle| \nu \right\rangle\,. \tag{33}$$

Clearly, the eigenvectors of L_z obtained from

$$L_z C_{l_z} = m_l S C_{l_z} \tag{34}$$

can be used to block-diagonalize $\mathbf{J}_z$ as given in Eq. (31), with the eigenvalues in $\mathbf{m}_j$ corresponding to $m_j = m_l \pm 1/2$:

$$\mathbf{C}^{\dagger}_{j_z} \mathbf{J}_z \mathbf{C}_{j_z} = \left(m_l \pm \frac{1}{2}\right)\mathbf{D}_{j_z}\,, \tag{35}$$

with $\mathbf{D}_{j_z}$ being a block-diagonal matrix in which all blocks correspond to one singular value of l and m_l. The eigenvectors of the $\mathbf{J}_z$ matrix are constructed as

$$\mathbf{C}_{j_z} = \begin{pmatrix} \mathbf{C}_{l_z^+} & \mathbf{0} \\ \mathbf{0} & \mathbf{C}_{l_z^-} \end{pmatrix}. \tag{36}$$

Within the parity blocks, we may now use this symmetry transformation to further block-diagonalize the Dirac Hamiltonian into blocks corresponding to the different m_j values

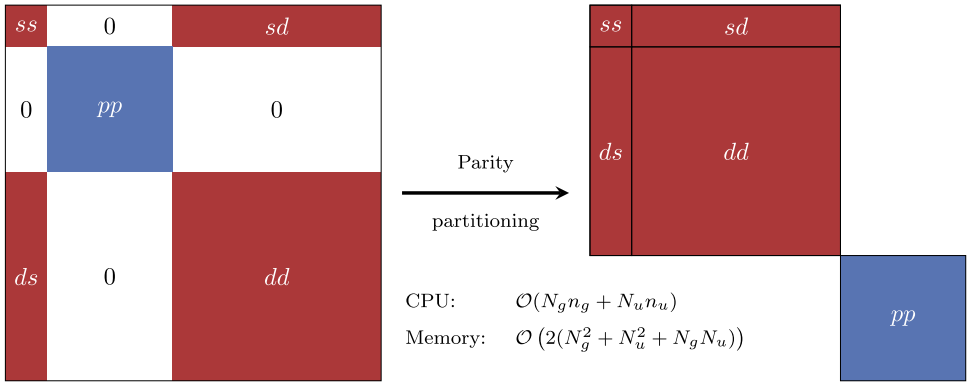

Fig. 1 Partitioning of the Hamiltonian into the *gerade* (red) and *ungerade* (blue) parity subspaces. N_g and N_u are the number of spherical harmonics $(s, p_x, p_y, p_z, \dots)$ within the subspaces while n_g and n_u are the number of function types $(s, p, d, \dots)$

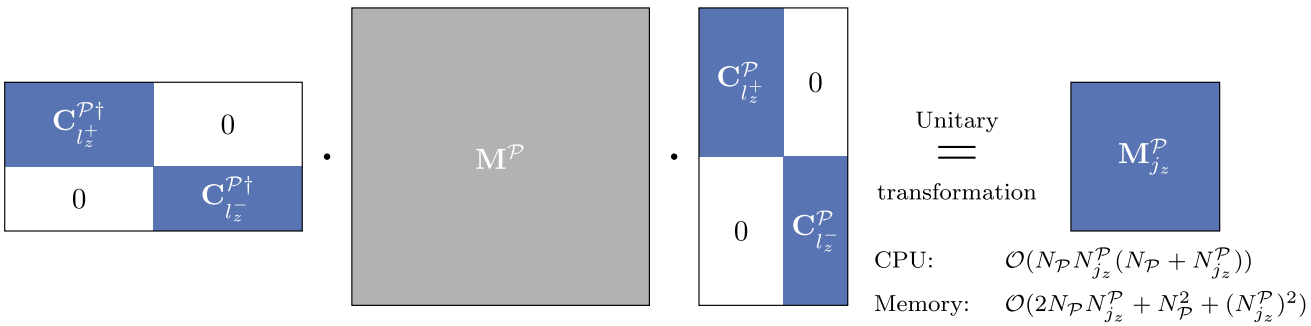

Fig. 2 Transformation of a parity block of the Hamiltonian $\mathbf{M}^{\mathcal{P}}$ to the j_z subspace. $N_{\mathcal{P}}$ is the size of the parity block and $N^{\mathcal{P}}_{j_z}$ is the size of the j_z subspace within the parity block

using the pre-computed eigenvectors $\mathbf{C}_{l_z^\pm}$. This is depicted in Fig. 2.

The matrix multiplications of this step constitute the slowest step in the entire calculation and thus the computational bottleneck in our current implementation.

2.6 Solving the Dirac equation

The symmetry-transformed Dirac Hamiltonian now has a block-diagonal form. The modified Dirac equation in the RMB condition can then be solved for each of these j_z blocks individually, all of which have the form given in Eq. (9). To ensure numerical stability, we use the approach of Peng et al. in Ref. [51], which was adapted to the finite magnetic field approach with the RMB condition by Sun and Li in Ref. [32]. To summarize, we first solve the eigenvalue problem of the overlap matrix:

$$\mathbf{S}^{\mathcal{P}}_{j_z}\mathbf{C}^{\mathrm{s}} = \mathbf{s}\mathbf{C}^{\mathrm{s}}\,, \tag{37}$$

where we have used the indices $\mathcal{P}$ and j_z to signify that this is done for every parity and j_z block separately. To ensure numerical stability, we eliminate eigenvectors corresponding to pseudo-linear degeneracies in the basis. This is done by constructing $\tilde{\mathbf{C}}^{\mathrm{s}} = \mathbf{s}^{-1/2}\mathbf{C}^{\mathrm{s}}$, setting $s_p = 0$ if it is below a threshold of 10^{-10}. All relevant matrices of the Dirac Hamiltonian are then transformed into the (possibly reduced) orthonormal basis of the overlap matrix:

$$\mathbf{M}^{\mathrm{s}} = \tilde{\mathbf{C}}^{\mathrm{s}\dagger}\mathbf{M}^{\mathcal{P}}_{j_z}\tilde{\mathbf{C}}^{\mathrm{s}}\,, \tag{38}$$

with $\mathbf{M} \in \{\mathbf{V}, \mathbf{\Pi}, \mathbf{W}\}$. Subsequently, the 2C eigenvalue equation

$$\mathbf{\Pi}^{\mathrm{s}}\mathbf{C}^{\tau} = \boldsymbol{\tau}\mathbf{C}^{\tau} \tag{39}$$

is solved and all relevant matrices of the Dirac Hamiltonian are transformed accordingly:

$$\mathbf{M}^{\tau} = \mathbf{C}^{\tau\dagger}\mathbf{M}^{\mathrm{s}}\mathbf{C}^{\tau}\,. \tag{40}$$

This procedure yields the following transformed Dirac Hamiltonian:

$$\tilde{\mathbb{H}}^{\mathrm{D}} = \begin{pmatrix} \mathbf{V}^{\tau} & c\sqrt{2\boldsymbol{\tau}} \\ c\sqrt{2\boldsymbol{\tau}} & \mathbf{W}^{\tau}(2\boldsymbol{\tau})^{-1} - 2c^2 \end{pmatrix}. \tag{41}$$

The energy eigenvalues of the Dirac equations are then obtained from solving the eigenvalue equation

$$\tilde{\mathbb{H}}^{\mathrm{D}}\tilde{\mathbb{C}} = \mathbb{E}\tilde{\mathbb{C}}\,, \tag{42}$$

since the transformed Dirac Hamiltonian $\tilde{\mathbb{H}}^{\mathrm{D}}$ is already in the orthonormal basis with respect to the relativistic metric. It should be emphasized again that the diagonalization

procedure described in this section is not a computational bottleneck due to our previous exploitation of the atomic symmetry in the presence of a magnetic field.

2.7 Non-relativistic limit

We close this section by briefly considering the non-relativistic limit. This will be utilized in Sect. 4.2 to compare data obtained for the hydrogen atom in an external magnetic field to the literature. We consider here the non-relativistic Schrödinger equation,

$$[\mathbf{\Pi} + \mathbf{V}]\,\mathbf{C}_p = E_p\,\mathbf{S}\mathbf{C}_p\,, \tag{43}$$

which can be reduced to a 1C equation if only magnetic fields parallel to the z-direction are considered:

$$[T + V]\,C_p = E_p\,SC_p\,. \tag{44}$$

The latter form is used in the context of this work. All eigenvalues are subsequently shifted by $\pm 0.5 B_z$ to account for the spin Zeeman contribution. Symmetry is considered similarly to the fully relativistic problem. First, the Hamiltonian is block-diagonalized with respect to inversion parity. Then, the eigenvectors obtained from Eq. (34) are used to further block-diagonalize the Hamiltonian with respect to m_l-symmetry. A canonical orthogonalization procedure is then used for each block, similar to the one described in Sect. 2.6. Since the metric consists only of the overlap matrix here, only the steps outlined in Eqs. (37) and (38) have to be considered. To ensure numerical stability, eigenvalues of the overlap matrix below a threshold of 10^{-10} are discarded.

3 Computational details

Large even-tempered basis sets were chosen such that chemical accuracy (errors of less than 1 kcal/mol $\approx 1.6 \cdot 10^{-3} E_\mathrm{h}$) can be obtained over a large window of magnetic field strengths, usually up to 1 B_0 for all investigated states. In the vast majority of cases, sub-chemical accuracy (errors of less than 0.1 kcal/mol $\approx 1.6 \cdot 10^{-4} E_\mathrm{h}$) [52, 53] is achieved. The basis set convergence was checked carefully, as shown in the Supporting Information. For the data presented in this work, we have thus chosen the basis sets detailed in Table 2.

Table 2 Information about the even-tempered basis sets used in this work. The limit l_max indicates the largest spherical harmonic used, with s-type functions being $l = 0$ and so forth. For all spherical harmonics, the same smallest exponent ζ_min and largest exponent ζ_max were used. Finally, Δ signifies the spacing between exponents according to Eq. (22)

Element	l_max	ζ_min	ζ_max	Δ
H	18	10^{-6}	10^{7}	2.0
Li^{2+}	11	10^{-6}	10^{8}	1.7
Na^{10+}	11	10^{-5}	10^{9}	1.7
K^{18+}	11	10^{-6}	10^{9}	2.0
Cu^{28+}	11	10^{-6}	10^{9}	2.0
Ag^{46+}	11	10^{-5}	10^{10}	2.0
Au^{78+}	10	10^{-5}	10^{10}	2.0
Rn^{85+}	6	10^{-5}	10^{10}	1.7

4 Results

Having discussed both the relevant theory and our implementation, we now present the results obtained for different relativistic hydrogen-like atoms in external magnetic fields. As mentioned above, we examine here the following systems: H, Li^{2+}, Na^{10+}, K^{18+}, Cu^{28+}, Ag^{46+}, Au^{78+}, and Rn^{85+}. For all of these, we compared our results to the analytic values in the absence of a magnetic field for the first, second, and third shells. Then, we investigated the field-dependence of these states. Finally, we analyzed basis set convergence in increasingly strong magnetic fields. This allows us to estimate the highest angular momentum quantum number l_max required for quantitative predictions. We show all results for the selected systems in the Supporting Information and focus on highlighting the more general trends here.

4.1 Field-free comparison to analytical results

To demonstrate the accuracy of our implementation, we first compare our results to the analytic values in the absence of a magnetic field. The energies corresponding to the electronic solutions of the Dirac equation for hydrogen-like atoms are given by the expression:

$$E_{n,k} = c^2 \left[1 + \left(\frac{Z\alpha}{n - |k| + \sqrt{k^2 - Z^2\alpha^2}} \right)^2 \right]^{-1/2} - c^2\,, \tag{45}$$

with α being the fine-structure constant. Therein, n is the principal quantum number and $k = j + 1/2$ where j is the total angular momentum quantum number. The energies calculated with Eq. (45) are compared to those obtained with our implementation in Table 3. For hydrogen, the error remains below $10^{-6} E_\mathrm{h}$ in all cases. This is two orders of magnitude more accurate than sub-chemical accuracy.

Moving on to heavier elements, we examine next the results obtained for the relativistic Cu^{28+} ion which are presented in Table 4. The energies are overall larger in magnitude compared to those of the relativistic hydrogen atom and the absolute errors are thus also larger. However, no errors larger

Table 3 Electronic solutions for the relativistic hydrogen atom in the absence of an external magnetic field. Here, our results for the lowest three shells are compared to the analytic values, alongside the difference ΔE

Level	This work in $[E_\mathrm{h}]$	Analytic value in $[E_\mathrm{h}]$	ΔE in $[E_\mathrm{h}]$
$1s_{1/2}$	−0.5000066841	−0.5000066566	$-2.75 \cdot 10^{-8}$
$2s_{1/2}$	−0.1250020773	−0.1250020802	$+2.91 \cdot 10^{-9}$
$2p_{1/2}$	−0.1250020564	−0.1250020802	$+2.38 \cdot 10^{-8}$
$2p_{3/2}$	−0.1250004004	−0.1250004160	$+1.56 \cdot 10^{-8}$
$3s_{1/2}$	−0.0555561630	−0.0555562952	$+1.32 \cdot 10^{-7}$
$3p_{1/2}$	−0.0555562217	−0.0555562952	$+7.35 \cdot 10^{-8}$
$3p_{3/2}$	−0.0555557324	−0.0555558021	$+6.96 \cdot 10^{-8}$
$3d_{3/2}$	−0.0555557752	−0.0555558021	$+2.68 \cdot 10^{-8}$
$3d_{5/2}$	−0.0555556123	−0.0555556377	$+2.54 \cdot 10^{-8}$

than $10^{-3}\ E_\mathrm{h}$ are found. As such, we are still more accurate than chemical accuracy in all cases, with most solutions being orders of magnitude more accurate than sub-chemical accuracy.

Finally, for very heavy elements such as the Rn^{85+} ion whose results are shown in Table 5, we do obtain errors slightly larger than $10^{-4}\ E_\mathrm{h}$ for certain levels such as $1s_{1/2}$, which are marginally worse than chemical accuracy. Higher levels are much more accurate, usually well above even sub-chemical accuracy. The deficiency for the very low-lying levels is a well-known artifact stemming from the point charge approximation, which requires extremely steep basis functions [54–56]. A finite nucleus approach eliminates this problem, and should be adopted for calculations on molecules containing heavy elements [57, 58]. We have not followed this approach here because a comparison with analytical values would then not have been possible.

Overall, the agreement between analytical results and those obtained from our approach is extremely good. The only deficiency we observed has already been attributed to a well-known problem originating from the point charge approximation for heavy elements. Otherwise, we obtain results with chemical accuracy or better in almost all cases. Data for the other one-electron systems is presented in the Supporting Information.

4.2 Validation of non-relativistic results for the hydrogen atom

Next, we compare the non-relativistic results for the hydrogen atom in an external magnetic field to those presented by Rösner et al. in Ref. [59]. Therein, a multi-configurational Hartree–Fock implementation was used to determine the energy levels of the different states. Selected magnetic field strengths in the range between $10^{-4}\ B_0$ and $10\ B_0$ were calculated therein in a basis of spherical harmonics. Furthermore, calculations employing a basis of Landau functions were used for higher field strengths. While newer implementations capable of calculating highly accurate solutions in very strong magnetic fields exist [60, 61], the work of Rösner et al. remains the most extensive benchmark we were able to find.

We start our discussion with the first and second shell of the hydrogen atom. Following the nomenclature of the $\mathcal{C}_{\infty h}$ point-group symmetry for an atom in an external magnetic field [45], the non-relativistic states can be associated with levels at zero field:

$$
\begin{aligned}
1s_0 &\rightarrow 1\Sigma_g, \\
2s_0 &\rightarrow 2\Sigma_g, \\
2p_{-1} &\rightarrow 1\Pi_u^+, \\
2p_0 &\rightarrow 1\Sigma_u,
\end{aligned}
$$

where the +/− superscript indicates a one-dimensional irreducible representation of $\mathcal{C}_{\infty h}$ that has a character of +i/−i under σ_h and that has been obtained from the corresponding two-dimensional irreducible representation of $\mathcal{D}_{\infty h}$. For example, $\Pi_u(\mathcal{D}_{\infty h}) \downarrow \mathcal{C}_{\infty h} = \Pi_u^+ \oplus \Pi_u^-$. Our results and those obtained from Ref. [59] are compared in Fig. 3. We have marked the difference ΔE for each state, indicating the accuracy of our reference ($10^{-6}\,E_\mathrm{h}$) in gray. For all four states shown here, we stay within this limit up until magnetic field strengths of approximately $1\ B_0$.

A general trend that can be observed is that low-lying states tend to be described more accurately by our method than higher states. This is noticeable by comparing the $1\Sigma_g$ and the $2\Sigma_g$ states in Figs. 3a and b, respectively. The $2\Sigma_g$ state shows a specific pattern at about $0.1\ B_0$, which is reproduced very well by our calculations. The origin of this feature is unclear—it resembles patterns one would expect from an avoided crossing, but no other state comes even remotely close at this field strength. At very high field strengths, well beyond $1\ B_0$, we observe a noticeable divergence between our calculations and those of Ref. [59]. In contrast, the other three states depicted here are accurate up to chemical accuracy even for field strengths up to $4\ B_0$.

Table 4 Electronic solutions for the relativistic Cu^{28+} ion in the absence of an external magnetic field. Here, our results for the lowest three shells are compared to the analytic values, alongside the difference ΔE

Level	This work in $[E_h]$	Analytic value in $[E_h]$	ΔE in $[E_h]$
$1s_{1/2}$	−425.31641989	−425.31642693	$+7.04 \cdot 10^{-6}$
$2s_{1/2}$	−106.63183856	−106.63185004	$+1.15 \cdot 10^{-5}$
$2p_{1/2}$	−106.63184036	−106.63185004	$+9.68 \cdot 10^{-6}$
$2p_{3/2}$	−105.42089639	−105.42090626	$+9.87 \cdot 10^{-6}$
$3s_{1/2}$	−47.256595711	−47.256774609	$+1.79 \cdot 10^{-4}$
$3p_{1/2}$	−47.256697003	−47.256774609	$+7.76 \cdot 10^{-5}$
$3p_{3/2}$	−46.897564093	−46.897647141	$+8.30 \cdot 10^{-5}$
$3d_{3/2}$	−46.897620406	−46.897647141	$+2.67 \cdot 10^{-5}$
$3d_{5/2}$	−46.780463446	−46.780490234	$+2.68 \cdot 10^{-5}$

Table 5 Electronic solutions for the relativistic Rn^{85+} ion in the absence of an external magnetic field. Here, our results for the lowest three shells are compared to the analytic values, alongside the difference ΔE

Level	This work in $[E_h]$	Analytic value in $[E_h]$	ΔE in $[E_h]$
$1s_{1/2}$	−4158.4183046	−4158.4243359	$+6.03 \cdot 10^{-3}$
$2s_{1/2}$	−1070.0941611	−1070.0952493	$+1.09 \cdot 10^{-3}$
$2p_{1/2}$	−1070.0951564	−1070.0952493	$+9.28 \cdot 10^{-5}$
$2p_{3/2}$	−948.45139903	−948.45139553	$-3.51 \cdot 10^{-6}$
$3s_{1/2}$	−461.41067503	−461.41100214	$+3.27 \cdot 10^{-4}$
$3p_{1/2}$	−461.41096418	−461.41100214	$+3.80 \cdot 10^{-5}$
$3p_{3/2}$	−425.13635279	−425.13635814	$+5.35 \cdot 10^{-6}$
$3d_{3/2}$	−425.13636326	−425.13635814	$-5.12 \cdot 10^{-6}$
$3d_{5/2}$	−415.48523001	−415.48522557	$-4.44 \cdot 10^{-6}$

For the third shell, comparisons to Rösner et al. [59] of the following states

$$
\begin{aligned}
3d_{-2} &\to 1\Delta_g^+, \\
3d_{-1} &\to 1\Pi_g^-, \\
3d_0 &\to 3\Sigma_g, \\
3s_0 &\to 4\Sigma_g,
\end{aligned}
$$

are shown in Fig. 4. The same pattern as before emerges. The lowest state of each symmetry is represented extremely well within our basis, particularly the $1\Delta_g^+$ and the $1\Pi_g^-$ states shown in Fig. 4a and b, respectively. For the latter, even those calculations at high field strengths for which Rösner et al. used a Landau basis (depicted here in green hollow points) are represented relatively well. This is however not the case for the $3\Sigma_g$ and $4\Sigma_g$ states shown in Fig. 4c and d. While they agree with the reference up to magnetic field strengths of about $0.1\,B_0$, they diverge heavily beyond this point. Clearly, for these higher states, a basis with higher angular momentum functions or a Landau basis would be needed. Overall, our basis seems to represent the non-relativistic states well in the presence of strong magnetic fields. Only at very high field strengths and for highly excited states do we get qualitative disagreements to the reference. However, it should be noted that the lowest states of a certain symmetry tend to be represented extremely well.

4.3 The relativistic mixing regime

In non-relativistic theory, strong magnetic fields are known to interact with the electronic structure in fascinating ways. This includes the formation of entirely new types of covalent bonds in the mixing regime, where Coulomb and magnetic interactions are of roughly the same magnitude [11, 20, 62]. As detailed above, relativistic theory gives rise to a new kind of mixing regime, which we shall investigate in the remainder of this work. To understand this better, it is helpful to consider the two perturbative limits.

First, if the internal magnetic interaction (in this case SOC) is much larger than the effects of an external magnetic field, we are in the limit of the anomalous Zeeman effect. Previously m_j-degenerate states are split up linearly, with lower m_j-states being favored energetically. We can examine this behavior for the Li^{2+} ion at field strengths of about $B = 10^{-5}\,B_0 \approx 1\,\mathrm{T}$, which is shown in Fig. 5a. Here, the effects of a magnetic field on the $2p$-orbitals are shown. In the absence of a magnetic field, they are split according to their j quantum numbers, with $j = 3/2$ being four-fold degenerate and higher in energy while $j = 1/2$ being two-fold degenerate and lower in energy. As a weak magnetic field is

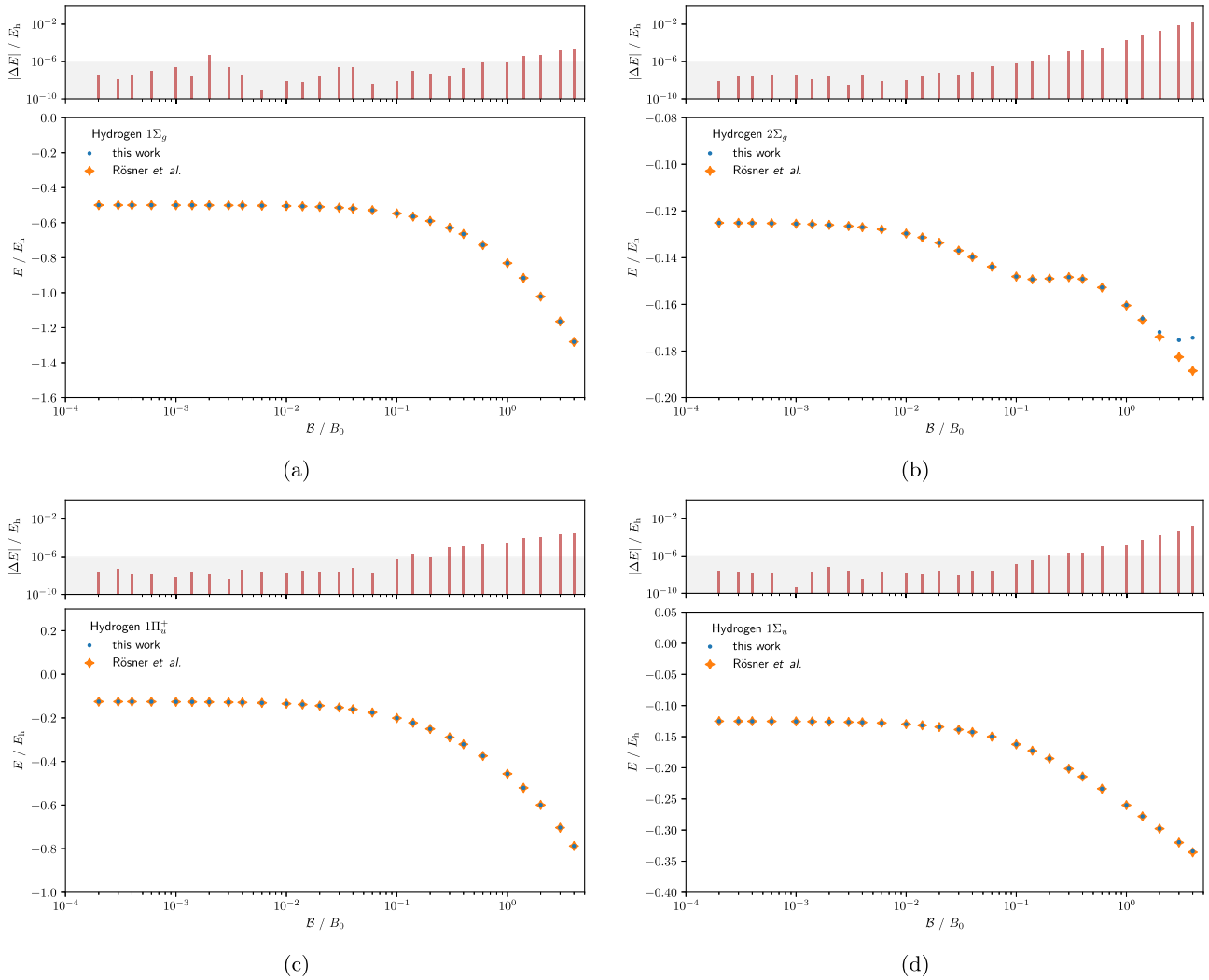

Fig. 3 Comparison between non-relativistic calculations performed in the context of this work and those performed by Rösner et al. in Ref. [59]. Shown here are deviations for the following states: **a** $1\Sigma_g$, **b** $2\Sigma_g$, **c** $1\Pi_u^+$, **d** $1\Sigma_u$. Reference values were accurate up to at most $10^{-6}\,E_h$, which is indicated in gray above the graphs

introduced, the states are clearly split according to their m_j values as expected.

In the other limit, the effects of an external magnetic field are much stronger than those of SOC. This is called the Paschen–Back limit where both angular momentum and spin are effectively decoupled again. Without consideration of anomalous g-factors, the splitting is exactly $m_l + 2m_s$, with m_l and m_s being angular momentum and spin projection quantum numbers, respectively. Thus, for the $2p$-orbitals shown in Fig. 5a, we observe five different lines in high field strengths, with $m_l = -1, m_s = 1/2$ and $m_l = 1, m_s = -1/2$ becoming degenerate in the Paschen–Back limit. This can be observed for very high field strengths as well in Fig. 5a, where these states remain degenerate, even once the diamagnetic terms are dominant. Only at very high field strengths is this degeneracy broken, which is a basis set artifact and not a real effect. We analyze the basis set convergence with respect to angular momentum l in the Supporting Information, where we observe that the unfilled points are not yet converged—even higher angular momentum basis functions would be needed to maintain the Paschen–Back degeneracy.

We are interested here in the mixing regime between the two limits. For Li^{2+}, this mixing regime is situated roughly between 1 and 100 T, as seen in Fig. 5a. But this is very dependent on the strength of SOC, as we will see later. With higher SOC, this is shifted to much higher field strengths. Thus, the relativistic mixing regime can be observed at different field strengths depending on both the system and the energy level. Importantly, this implies that it may be found at ambient magnetic field strengths in the valence shell of atomic

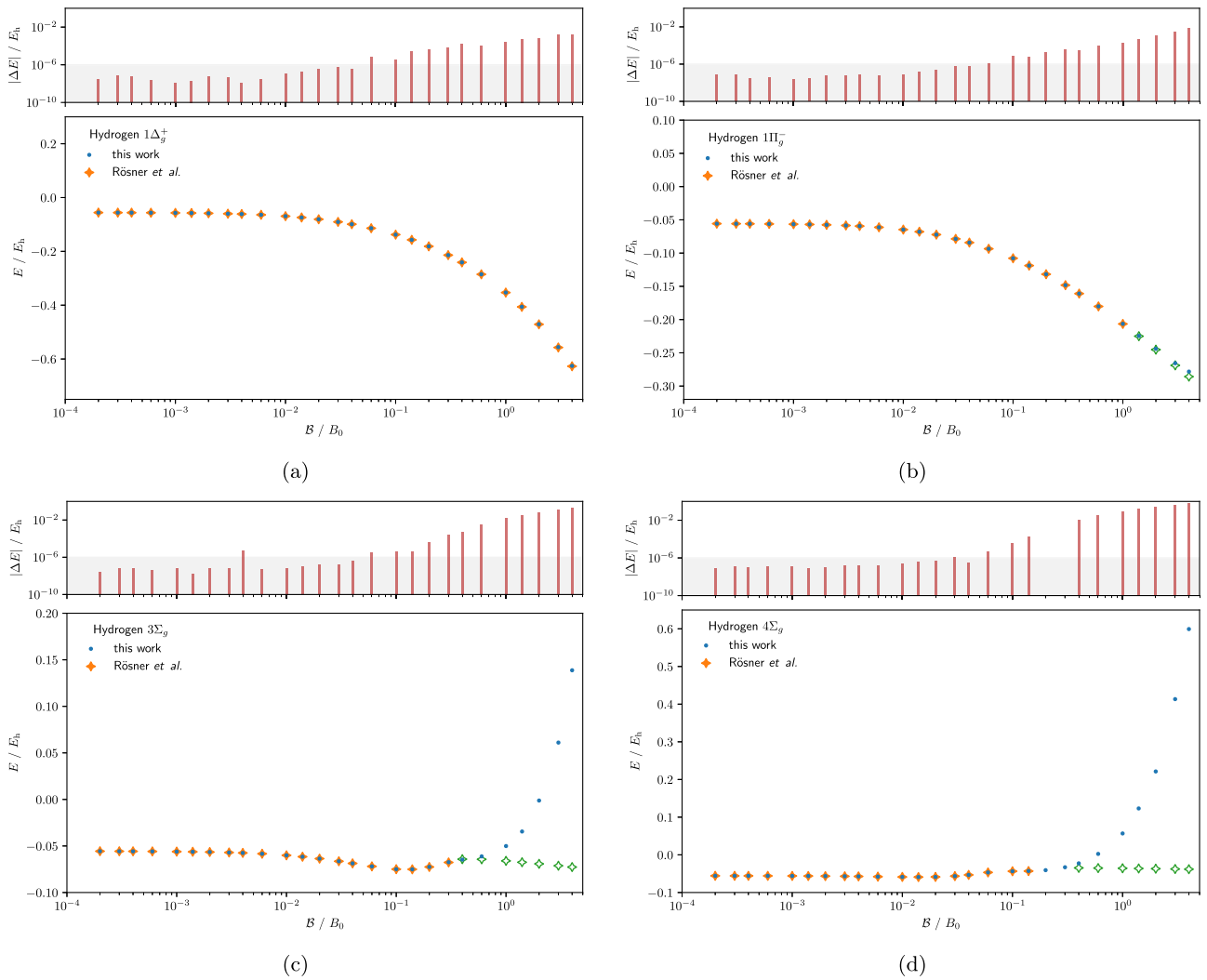

Fig. 4 Comparison between non-relativistic calculations performed in the context of this work and those performed by Rösner et al. in Ref. [59]. Shown here are deviations for the following states: **a** $1\Delta_g^+$, **b** $1\Pi_g^-$, **c** $3\Sigma_g$, and **d** $4\Sigma_g$. Reference values were accurate up to at most $10^{-6}\ E_h$, which is indicated in gray above the graphs

and molecular systems, particularly for structures containing heavier elements.

4.4 Spin-orbit-induced avoided crossing

Another important feature emerges in the presence of both SOC and external magnetic fields. Compared to non-relativistic calculations, the fermionic symmetry can lead to the emergence of avoided crossings. We show this explicitly for the hydrogen atom in Fig. 6, where both the non-relativistic and relativistic results are compared. In particular, we observe a crossing of the non-relativistic $1\Pi_u^+$ and $2\Sigma_u$ states at a magnetic field strength of about $0.15883\ B_0$ as these two states have different symmetries. On the other hand, in the presence of relativistic effects, both states turn out to have the same $E^-_{1/2,u}$ character due to SOC. As such, they can interact with each other and we observe a (slightly shifted) avoided crossing instead.

Importantly, this avoided crossing is relatively weak here, and the curves come very close to one another. This follows directly from the decomposition of the Hamiltonian shown in Eq. (2) and the relatively weak SOC contribution. For hydrogen, the Hamiltonian can be approximated as non-relativistic, and only a small spin-orbit perturbation is then added. Only the perturbative part alters the symmetry, and thus the separation between the two $E^-_{1/2,u}$-states is approximately the SOC energy. This is in alignment with the results presented in Table 3 when compared to the non-relativistic analytic solutions, and it has been observed in the perturbative limit before [63].

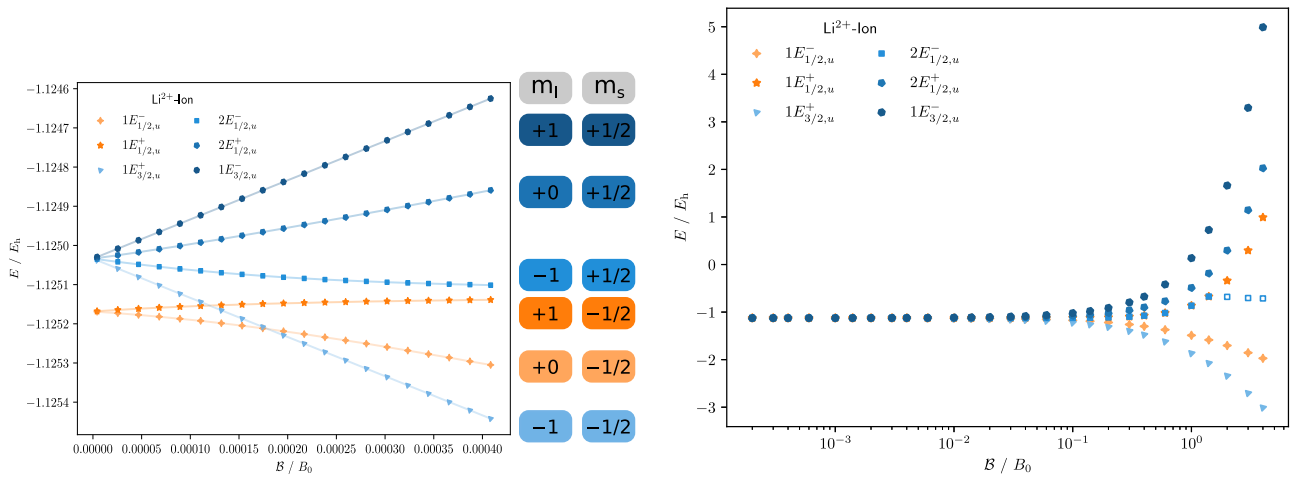

Fig. 5 **a** Transition from the anomalous Zeeman limit to the Paschen–Back limit for the Li^{2+} ion. **b** Transition from the Coulomb regime to the Landau regime for Li^{2+}. Unfilled data points denote calculations that are not converged with respect to angular momentum

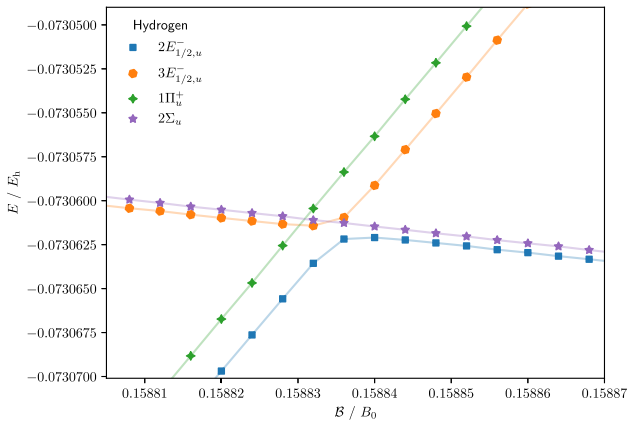

Fig. 6 Spin-orbit-induced avoided crossing for hydrogen in a strong magnetic field. The two states $1\Pi_u^+$ and $2\Sigma_u$ are allowed to cross in the non-relativistic case because they are characterized by different irreducible representations. In the presence of SOC, these symmetries are altered and both states end up with the same $E_{1/2,u}^-$ character. Thus the curves are no longer allowed to cross

Importantly, the features of the two states $1\Pi_u^+$ and $2\Sigma_u$ are very different in the non-relativistic limit. They have very different basis set requirements as previously discussed in Sect. 4.2. This is also specifically shown in the Supporting Information: $2\Sigma_u$ requires many more higher angular momentum functions in its basis than $1\Pi_u^+$ does. Even though the two $E_{1/2,u}^-$-states never cross in the relativistic calculations, this feature is still observed. Beyond the avoided crossing, the $2E_{1/2,u}^-$ state suddenly requires many more higher angular momentum functions, while $3E_{1/2,u}^-$ suddenly requires much less.

4.5 Heavy elements in strong magnetic fields

Examining heavier elements such as Na^{10+} and K^{18+}, we observe that the transition between the anomalous Zeeman effect and the Paschen–Back limit is shifted to higher magnetic field strengths. This is shown in Fig. 7. Furthermore, we notice an interesting detail: the diamagnetic contributions already become relevant for the non-linear interaction between SOC and the external magnetic field. This results in a new type of mixing regime governed by the strength of all internal and external magnetic contributions, which scale differently with respect to both SOC and magnetic field strength.

For even heavier elements such as Cu^{28+}, Ag^{46+}, Au^{78+}, and Rn^{85+}, the SOC becomes increasingly larger as depicted in Fig. 8. For the latter three systems, no crossings are observed even up until very strong field strengths of $10\,B_0$ for the states investigated here. The SOC is so much stronger than the external magnetic contribution that it remains the dominating effect. For core levels of heavy elements, the magnetic field remains a perturbative contribution.

An important implication follows from the knowledge that, for heavy elements, external magnetic fields affect mostly valence shells while leaving core levels relatively untouched. Core levels of heavy elements are often implicitly described using relativistic effective core potentials (RECP), which assume that the electronic structure of the core remains atomic-like upon molecule formation. Since these core levels are not affected much by very strong external magnetic fields, this approximation is likely still extremely good for all field strengths one would need to consider in practice—for instance those found in magnetic white dwarfs [29]. As such, it might be possible to avoid having to do very costly four- or two-component calculations for most applications. Instead,

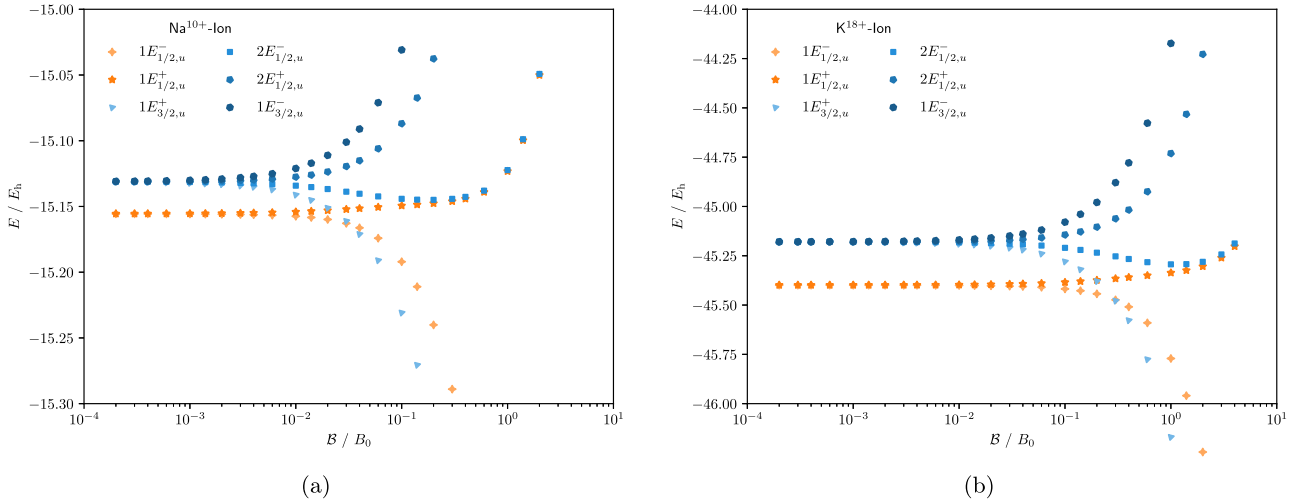

Fig. 7 Transition from the anomalous Zeeman limit to the Paschen–Back and Landau limits for **a** Na^{10+} and **b** K^{18+}

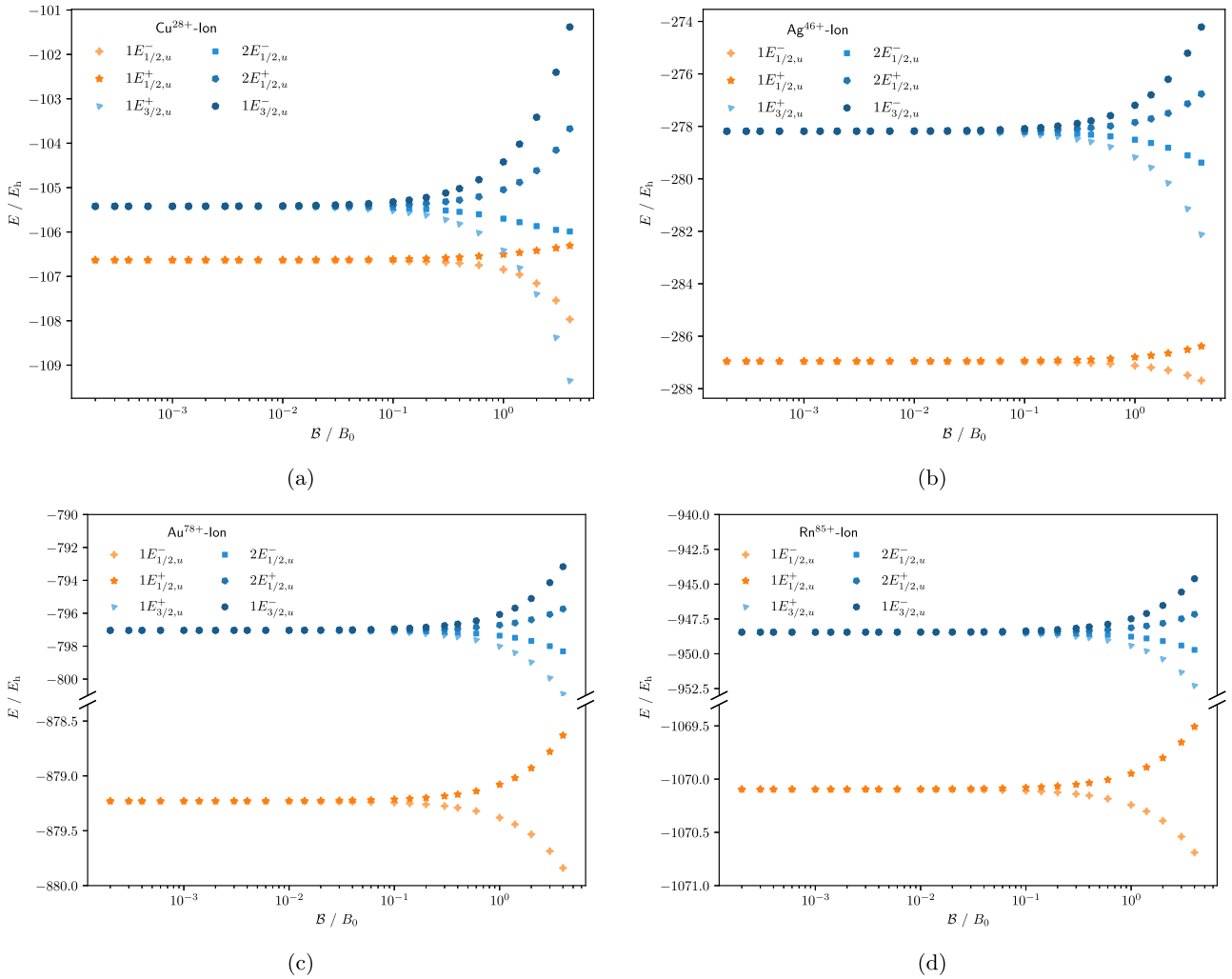

Fig. 8 Transition from the anomalous Zeeman limit to the Paschen–Back and Landau limits for **a** Cu^{28+}, **b** Ag^{46+}, **c** Au^{78+}, and **d** Rn^{85+}

one could simply implement the necessary RECP terms in a ff/LAO framework and continue to work in an otherwise non-relativistic framework.

5 Conclusion

In this work, we have derived and implemented a numerical framework capable of solving the Dirac equation for relativistic hydrogen-like atoms in finite magnetic fields. The implementation is based on Gaussian-type orbitals and employs the restricted magnetic balance condition to avoid variational collapse. Fermionic symmetry is exploited to accelerate the otherwise costly calculations and in order to separate states of different symmetry. We confirmed the validity of our implementation by comparing against analytical values for various relativistic hydrogen-like atoms in the absence of a magnetic field. Furthermore, we compared to non-relativistic results obtained for hydrogen in the presence of a magnetic field. This demonstrated that our implementation is indeed accurate up to very high field strengths. Only highly excited states are not captured well in field strengths beyond 1 B_0.

The main goal of this work was then to investigate the mixing regime between the anomalous Zeeman and the Paschen–Back limit for increasingly heavy hydrogen-like atoms. With increasing field strengths, we observed both spin-orbit-induced avoided crossings and conical intersections. Furthermore, as the strength of spin-orbit coupling increases, diamagnetic terms start to become more prevalent already within the mixing regime, indicating that Coulomb interactions, relativistic effects, and external magnetic fields are of similar strengths. Finally, heavy elements exhibit such strong spin-orbit coupling strengths that even very strong magnetic fields can be considered to be small perturbations. This is predominantly the case for core levels of heavier elements, and it implies that relativistic effective core potentials are likely well-suited to be used even in very strong magnetic fields. If this is indeed the case, calculations on heavy elements in strong magnetic fields will be much less computationally demanding, and investigations along these lines will thus be the subject of future work.

Supplementary material

An electronic Supporting Information is available. It contains further data for all systems, including plots of the electronic energy vs. the magnetic field strength, information about the basis set convergence, and a derivation for the characters of spinors in $\mathcal{C}_{\infty h}$.

Supplementary Information The online version contains supplementary material available at https://doi.org/10.1007/s00214-026-03288-8.

Author Contributions All authors were responsible for the conceptualization. BM and AP wrote the software and BM was mainly responsible for producing the data. BM also prepared all figures. BCH was mainly responsible for the symmetry discussions and prepared Table I. AP wrote the majority of the article, with BCH writing chapter 2.4 and chapter 2 of the Supporting Information. LV was responsible for deriving the symmetry transformation technique in chapter 2.5, as well as helping with this important part of the software. All authors reviewed and edited the article and its SI carefully.

Funding AP gratefully acknowledges support from the Walter Benjamin Programme funded by the Deutsche Forschungsgemeinschaft (DFG, German Research Foundation) through DFG-529675149. BCH thanks New College, University of Oxford for funding from the Oglander Fellowship.

Data Availability The data that support the findings of this study are available within the article and its supplementary material. We make all data computed and used in this study publicly available on a file share provider https://bwsyncandshare.kit.edu/s/YXeNswztrfSSQmC. The dataset can be processed, and visualized with the scripts provided at https://github.com/Apollon0212/analysis_The_relativistic_hydrogen-like-atom_in_a_finite_magnetic_field.git. The code used for the calculations presented in this work is available at https://github.com/Apollon0212/ffasterOEA.git.

Declarations

Conflict of interest The authors declare no conflict of interest.

References

1. Zeeman P (1897) Lond Edinb Dublin Philos Mag J Sci 43:226
2. London F (1937) J Phys Radium 8:397. https://doi.org/10.1051/jphysrad:01937008010039700
3. Stormer HL (1999) Rev Mod Phys 71:875. https://doi.org/10.1103/RevModPhys.71.875
4. Duncan RC (2000) in AIP Conf. Proc., (AIP, Huntsville, Alabama (USA)) 526:830–841 https://doi.org/10.1063/1.1361651
5. Yoshioka D (2002) The Quantum Hall Effect. Berlin Heidelberg, Springer
6. Douçot B, Pasquier V (2005) in The Quantum Hall Effect: Poincaré Seminar 2004, edited by Douçot B, Pasquier V, Duplantier B, Rivasseau V (Birkhäuser, Basel) 23–53 https://doi.org/10.1007/3-7643-7393-8_2
7. Schulten K (1982) in Festkörperprobleme 22: Plenary Lectures of the 46th Annual Meeting of the German Physical Society (DPG) and of the Divisions "Semiconductor Physics" "Metal Physics" "Low Temperature Physics" "Thermodynam-

ics and Statistical Physics" "Thin Films" "Surface Physics" "Magnetism"Münster, March 29–April 2, 1982, edited by P. Grosse Aachen (Springer, Berlin, Heidelberg) pp 61–83 https://doi.org/10.1007/BFb0107935
8. Steiner UE, Ulrich T (1989) Chem Rev 89:51. https://doi.org/10.1021/cr00091a003
9. Grissom CB (1995) Chem Rev 95:3. https://doi.org/10.1021/cr00033a001
10. Buchachenko A, Lawler RG (2017) Acc Chem Res 50:877. https://doi.org/10.1021/acs.accounts.6b00608
11. Stopkowicz S (2018) Int J Quantum Chem 118:e25391. https://doi.org/10.1002/qua.25391
12. Ditchfield R (1974) Mol Phys 27:789. https://doi.org/10.1080/00268977400100711
13. Helgaker T, Jørgensen P (1991) J Chem Phys 95:2595. https://doi.org/10.1063/1.460912
14. Gauss J, Ruud K, Helgaker T (1996) J Chem Phys 105:2804. https://doi.org/10.1063/1.472143
15. Hennum AC, Klopper W, Helgaker T (2001) J Chem Phys 115:7356. https://doi.org/10.1063/1.1405009
16. Autschbach J (2011) ChemPhysChem 12:3224. https://doi.org/10.1002/cphc.201100225
17. Franzke YJ, Holzer C (2023) J Chem Phys 159:184102. https://doi.org/10.1063/5.0171509
18. Tellgren EI, Soncini A, Helgaker T (2008) J Chem Phys 129:154114. https://doi.org/10.1063/1.2996525
19. Becken W, Schmelcher P, Diakonos FK (1999) J Phys B: At Mol Opt Phys 32:98721. https://doi.org/10.1088/0953-4075/32/6/018
20. Lange KK, Tellgren EI, Hoffmann MR, Helgaker T (2012) Science 337:327. https://doi.org/10.1126/science.1219703
21. Pemberton MJ, Irons TJP, Helgaker T, Teale AM (2022) J Chem Phys 156:204113. https://doi.org/10.1063/5.0092520
22. Franzke YJ, Pausch A, Holzer C (2025) J Chem Phys 162. https://doi.org/10.1063/5.0246433
23. Blaschke S, Kitsaras MP, Stopkowicz S (2024) Phys Chem Chem Phys 26:28828. https://doi.org/10.1039/D4CP03103B
24. Kronenberger ML, Steinmetz D, Appenzeller A, Pausch A (2025) J Chem Phys 163:224114. https://doi.org/10.1063/5.0300324
25. Steinmetz D, Pausch A (2025) J Chem Phys 162:154109. https://doi.org/10.1063/5.0261461
26. Stopkowicz S, Gauss J, Lange KK, Tellgren EI, Helgaker T (2015) J Chem Phys 143. https://doi.org/10.1063/1.4928056
27. Monzel L, Pausch A, Peters LDM, Tellgren EI, Helgaker T, Klopper W (2022) J Chem Phys 157:054106. https://doi.org/10.1063/5.0097800
28. Blaschke S, Stopkowicz S, Pausch A (2024) J Chem Phys 161:024117. https://doi.org/10.1063/5.0217246
29. Hollands MA, Stopkowicz S, Kitsaras MP, Hampe F, Blaschke S, Hermes JJ (2023) Mon Not R Astron Soc 520:3560. https://doi.org/10.1093/mnras/stad143
30. Breit G, Rabi II (1931) Phys Rev 38:2082. https://doi.org/10.1103/PhysRev.38.2082.2
31. Tang D, Sun S, Li X (2024) J Chem Theory Comput 20:9917. https://doi.org/10.1021/acs.jctc.4c01028
32. Sun S, Li X (2020) J Chem Theory Comput 16:4533. https://doi.org/10.1021/acs.jctc.0c00287
33. Reynolds RD, Shiozaki T (2015) Phys Chem Chem Phys 17:14280. https://doi.org/10.1039/C4CP04027A
34. Lehtola S, Dimitrova M, Sundholm D (2020) Mol Phys 118:e1597989. https://doi.org/10.1080/00268976.2019.1597989
35. Farhaz R, Bischoff FA, Blaschke S, Stopkowicz S (2025) J Chem Phys 163:034308. https://doi.org/10.1063/5.0274736
36. Komorovský S, Repiský M, Malkina OL, Malkin VG, Malkin Ondík I, Kaupp M (2008) J Chem Phys 128:104101. https://doi.org/10.1063/1.2837472
37. Cheng L, Xiao Y, Liu W (2009) J Chem Phys 131:244113. https://doi.org/10.1063/1.3283036
38. Komorovský S, Repiský M, Malkina OL, Malkin VG (2010) J Chem Phys 132:154101. https://doi.org/10.1063/1.3359849
39. Ditchfield R (1972) J Chem Phys 56:5688. https://doi.org/10.1063/1.1677088
40. Dahle P, Ruud K, Helgaker T, Taylor PR (1999) in Pauling's Legacy, Theoretical and Computational Chemistry, Vol. 6, edited by Z. Maksi? and W. Orville-Thomas (Elsevier) pp. 147–188 https://doi.org/10.1016/S1380-7323(99)80008-9
41. Pausch A, Klopper W (2020) Mol Phys 118:e1736675. https://doi.org/10.1080/00268976.2020.1736675
42. Schlegel HB, Frisch MJ (1995) Int J Quantum Chem 54:83. https://doi.org/10.1002/qua.560540202
43. Ceulemans AJ (2013) Group Theory Applied to Chemistry (Springer Netherlands)
44. Altmann S (1979) Mol Phys 38:489. https://doi.org/10.1080/00268977900101831
45. Pausch A, Gebele M, Klopper W (2021) J Chem Phys 155. https://doi.org/10.1063/5.0069859
46. Huynh BC, Wibowo-Teale M, Wibowo-Teale AM (2024) J Chem Theory Comput 20:114. https://doi.org/10.1021/acs.jctc.3c01118
47. Altmann SL (2005) Rotations, Quaternions, and Double Groups (Dover Publications, Mineola, New York, USA)
48. Strange P (1998) Relativistic Quantum Mechanics: With Applications in Condensed Matter and Atomic Physics (Religious Studies; 47) (Cambridge University Press, Cambridge) https://doi.org/10.1017/CBO9780511622755
49. Dyall KG, Faegri K Jr (2007)Introduction to Relativistic Quantum Chemistry (Oxford University Press, Inc., New York, USA)
50. Saue T, Jensen HJA (1999) J Chem Phys 111:6211. https://doi.org/10.1063/1.479958
51. Peng D, Middendorf N, Weigend F, Reiher M (2013) J Chem Phys 138. https://doi.org/10.1063/1.4803693
52. Schuurman MS, Muir SR, Allen WD, Schaefer HF (2004) J Chem Phys 120:11586. https://doi.org/10.1063/1.1707013
53. Dubecký M, Jurečka P, Derian R, Hobza P, Otyepka M, Mitas L (2013) J Chem Theory Comput 9:4287. https://doi.org/10.1021/ct4006739
54. Andrae D (2000) Phys Rep 336:413. https://doi.org/10.1016/S0370-1573(00)00007-7
55. Andrae D, Reiher M, Hinze J (2000) Chem Phys Lett 320:457. https://doi.org/10.1016/S0009-2614(00)00068-3
56. Mastalerz R, Widmark P-O, Roos BO, Lindh R, Reiher M (2010) J Chem Phys 133:144111. https://doi.org/10.1063/1.3491239
57. Visscher L, Dyall KG (1997) At Data Nucl Data Tables 67:207. https://doi.org/10.1006/adnd.1997.0751
58. Dyall KG, Faegri K Jr (1993) Chem Phys Lett 201:27. https://doi.org/10.1016/0009-2614(93)85028-M
59. Rösner W, Wunner G, Herold H, Ruder H (1984) J Phys B Atom Mol Phys 17:29. https://doi.org/10.1088/0022-3700/17/1/010
60. Baye D, Vincke M, Hesse M (2008) J Phys B 41:055005. https://doi.org/10.1088/0953-4075/41/5/055005
61. Schimeczek C, Wunner G (2014) Astrophys J 212. https://doi.org/10.1088/0067-0049/212/2/26
62. Austad J, Borgoo A, Tellgren EI, Helgaker T (2020) Phys Chem Chem Phys 22:23502. https://doi.org/10.1039/D0CP03259J
63. Poszwa A, Rutkowski A (2004) Phys Rev A 69:023403. https://doi.org/10.1103/PhysRevA.69.023403